ELSEVIER

Nuclear Instruments and Methods in Physics Research A 457 (2001) 203–211

NUCLEAR INSTRUMENTS & METHODS IN PHYSICS RESEARCH Section A

www.elsevier.nl/locate/nima

Evaluation of a Compton scattering camera using 3-D position sensitive CdZnTe detectors

Y.F. Du*, Z. He, G.F. Knoll, D.K. Wehe, W. Li

Department of Nuclear Engineering and Radiological Science, The University of Michigan, Ann Arbor, MI 48109, USA

Received 22 May 2000; accepted 15 June 2000

Abstract

A CZT Compton Camera (CCC) is being built using two three-dimensional (3-D) position-sensitive CZT detectors. Expected system performance was analyzed by analytical and Monte Carlo approaches. Based on the measurement of detector energy and position resolution, the expected angular resolution is $\sim 3^\circ$ and $\sim 2^\circ$ for a $\pm 30^\circ$ FOV for 511 keV and 1 MeV γ-rays, respectively. The intrinsic efficiency for a point source 10 cm from the first detector surface ranges from 1.5×10^{-4} to 8.8×10^{-6} for 500 keV–3 MeV.

Keywords: Compton scatter imaging; 3-D position sensitive; Room-temperature CZT detector

1. Introduction

Compton cameras have potential as radiation imagers in environmental remediation, as survey devices for nuclear industrial sites, and in nuclear treaty verification, and medical imaging applications. These applications are best served by portable devices. However, previous Compton cameras have used high-purity germanium (HPGe), or silicon detectors combined with scintillation detectors. Their portability is limited by either the requirement for cryogenic cooling of the semiconductor detectors, or the relatively large volume of the photomultiplier tubes. In contrast, CdZnTe detectors can be operated at room temperature, can achieve high energy and position resolution compared to scintillation detectors, and can be made compact. The three-dimensional (3-D) position-sensitive CZT detectors have recently demonstrated a 1.7% FWHM energy resolution at 662 keV and a 1 mm position resolution [1]. These are attractive for portable Compton scattering cameras in the energy region of several hundred keV to a few MeV.

In this paper, we present the expected performance of a prototype Compton scattering camera based on two 1 cm^3 cubic 3-D position-sensitive CZT detectors. The energy resolution, angular resolution and the efficiency of the camera have been analyzed. A list-mode maximum likelihood iterative reconstruction algorithm is used. Monte Carlo methods are used to verify our analytical predictions and the implementation of the reconstruction algorithm. Based on our measured detector energy and position resolution, the overall camera performance is predicted from these simulations and operating system parameters, such as the

* Corresponding author. Tel. +1-734-936-0127; fax: +1-734-763-4540.

E-mail address: yfdu@engin.umich.edu (Y.F. Du).

0168-9002/01/$ - see front matter
PII: S0168-9002(00)00669-0

separation distance and central scattering angle between the two detectors, are suggested.

2. Proposed system overview

As shown in Fig. 1, the proposed prototype Compton scattering camera is composed of two 1 cm^3 cubic 3-D position-sensitive CZT detectors. There are 11×11 pixels on each anode surface. The signals from the anode pixels are read out by integrated VA chips with independent signal processing channels. For each γ interaction, the energy and lateral (x, y) position information are determined by the anode pixel signal, and the depth (z) information is given by the ratio of the signals from the cathode and the anode pixel. More details about 3-D position-sensitive CZT detectors are given in Ref. [1]. Since there is only one second detector for this prototype Compton scattering camera, the whole system or the second detector must rotate around the z-axis of the first detector for adequate sampling.

3. Performance estimation

In this section, we calculate the expected key performance parameters: the angular resolution and intrinsic efficiency.

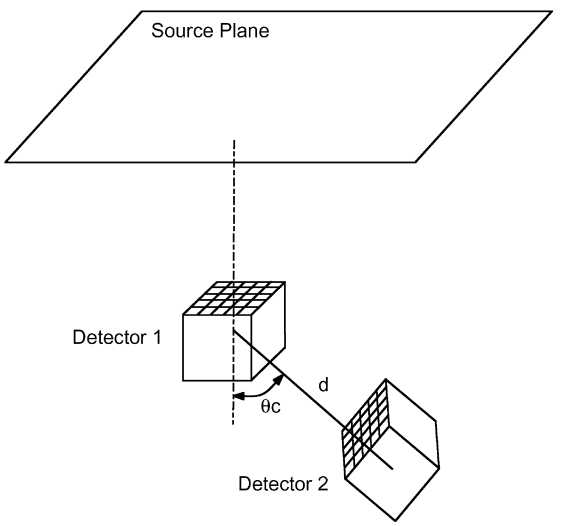

Fig. 1. CCC system setup.

3.1. Angular resolution

In Compton scatter imaging, the incident radiation Compton scatters in the first detector and the scattered photon is detected by the second detector. The source location can be backprojected to lie the surface of a cone. The cone's axis is defined by the interaction locations in the two detectors, and the cone angle θ is determined from the Compton equation as

$$\cos\theta = 1 - \frac{m_e c^2 E_e}{E_0^2 - E_0 E_e} \tag{1}$$

where E_0 is the incident energy (assumed known), E_e is the energy deposited in the first detector and m_e is the electron mass. Any energy uncertainty for E_e due to either the first detector energy resolution or the Doppler broadening effect, as well as any measurement position uncertainty, will lead to an angular uncertainty of the source location. The overall angular resolution is the quadratic summation of three components [2]

$$\tan^2(\Delta\theta_{\text{overall}}) = \tan^2(\Delta\theta_{\text{energy-resolution}}) + \tan^2(\Delta\theta_{\text{Doppler}}) + \tan^2(\Delta\theta_{\text{geometry}}) \tag{2}$$

where $\Delta\theta_{\text{energy-resolution}}$ is the detector energy resolution contribution, $\Delta\theta_{\text{Doppler}}$ is the Doppler broadening contribution and $\Delta\theta_{\text{geometry}}$ is the detector position resolution contribution.

Using error propagation from Eq. (1), the energy uncertainty contribution to angular uncertainty is given by

$$\Delta\theta_{\text{energy}} = \frac{(1 + \alpha(1 - \cos\theta))^2}{E_0 \alpha \sin\theta}\Delta E \tag{3}$$

where $\alpha = E_0/m_e c^2$. Our first step is thus to examine contributions from detector energy resolution and Doppler broadening.

3.1.1. Detector energy resolution contribution

For our 3-D position-sensitive CZT detectors, the energy resolution at several incident γ energies is shown in Fig. 2. The electronic noise is around 6–7 keV using the current readout system. By fitting the measured data points in Fig. 2, the general

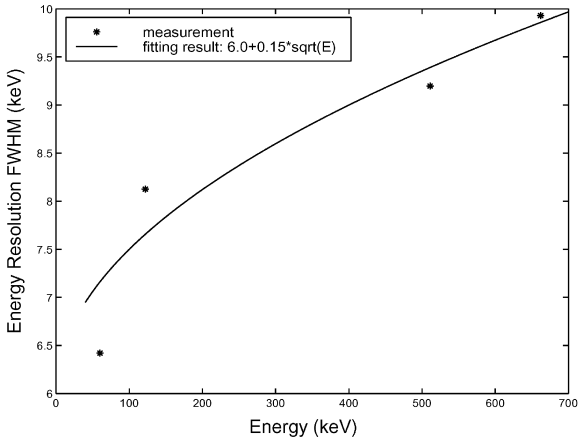

Fig. 2. 3-D CZT detector energy resolution.

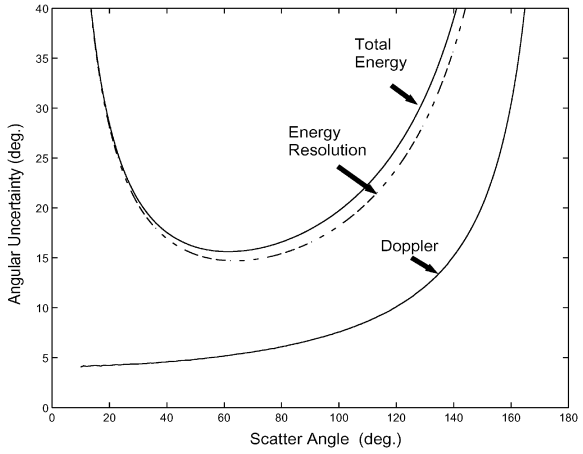

Fig. 3. Angular uncertainty due to detector energy resolution and Doppler broadening at 114 keV.

relationship between energy resolution and the incident energy is given by $\Delta E = 6.0 + 0.15\sqrt{E}$. Using Eq. (3), the predicted angular resolution due to the first detector energy resolution for a 114 keV γ is shown in Fig. 3. Since $\Delta\theta_{\text{energy-resolution}}$ is larger than 15° for all scattering angles, the CZT detector is not useful as the first detector for low-energy Compton scatter imaging. But as shown in Fig. 4(a) for a 511 keV γ, the $\Delta\theta_{\text{energy-resolution}}$ is only 2–3° for scattering angles between 20° and 80°, and decreases as the incident energy increases. As shown in Fig. 4(b), $\Delta\theta_{\text{energy-resolution}}$ is only about 1° for a 1 MeV with 20–80° scattering angles.

3.1.2. Doppler broadening contribution

The derivation of Eq. (1) is based on the assumption that the electron is free and at rest before the scattering interaction. But in reality, bound electrons have finite momenta. If the electron momentum $\boldsymbol{p}$ is included, the energy transferred to the electron by the incident photon is given by [3]

$$E_e = \frac{|\boldsymbol{k}|^2}{2m_e} + \frac{\boldsymbol{k}\cdot\boldsymbol{p}}{m_e} = \frac{|\boldsymbol{k}|^2}{2m_e} + \frac{|\boldsymbol{k}|p_z}{m_e} \tag{4}$$

where the scattering vector $\boldsymbol{k} = \boldsymbol{k}_1 - \boldsymbol{k}_0$ is the momentum difference between the scattered and incident photons, and p_z is the initial electron momentum along the scattering vector direction. In Eq. (4), the first term on the right-hand side is the usual term given by the Compton equation, and the second term is the Doppler shift, which is linear in p_z, and increases with incident energy E_0. So the scattered photon energy is not only determined by scattering angle θ, but also depends on the coupling between scattering vector $\boldsymbol{k}$ and the initial electron momentum $\boldsymbol{p}$. The energy distribution of the scattered photons is given by the double differential cross-section [4]

$$\frac{d^2\sigma}{d\Omega\, dE_1} = \tfrac{1}{2}m_e r_0^2 (E_c^2 + E_1^2 - 2E_c E_1 \cos\theta)^{1/2} \times \left(\frac{E_1}{E_0}\right)\left(\frac{E_1}{E_0} + \frac{E_0}{E_1} - \sin^2\theta\right) J(p_z) \tag{5}$$

where E_c is the scattered photon energy calculated by the Compton equation, r_0 is the classical electron radius, and the Compton profile $J(p_z)$ is the electron momentum distribution. At a fixed scattering angle θ, the scattered photon energy distribution is mainly determined by the Compton profile $J(p_z)$, because the other terms are relatively slowly varying with E_1.

Neglecting the small chemical and lattice effects on the electron momentum distribution in crystals, the calculated FWHM energy spread due to Doppler broadening is shown in Fig. 5 for 511 keV and 1 MeV γ-rays. These results are based on the calculated Compton profiles in Ref. [5].[1] From Fig. 5,

[1] For $Cd_{0.8}Zn_{0.2}Te$, average atomic Compton profile is derived from that for Cd, Zn and Te.

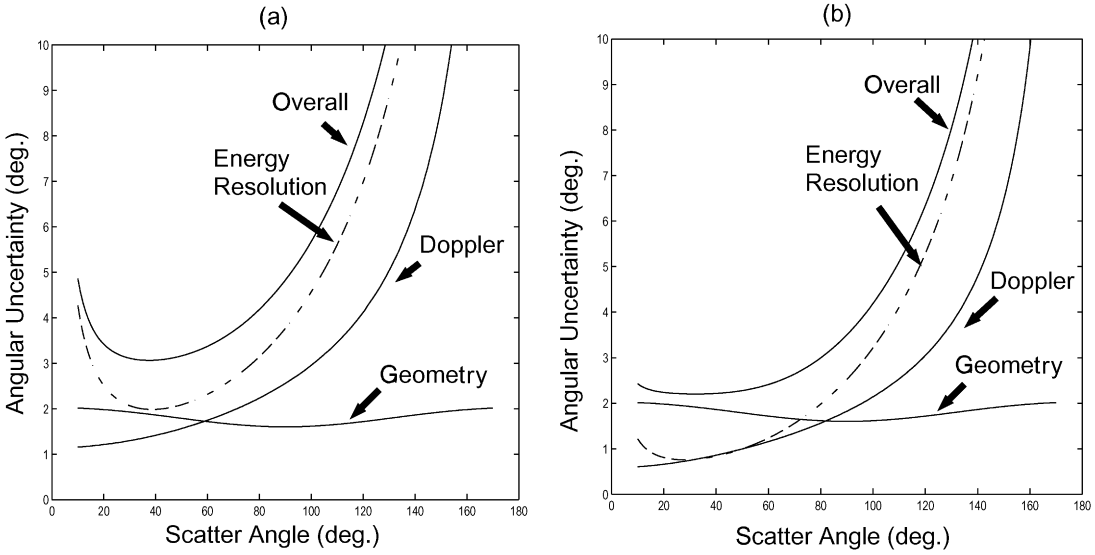

Fig. 4. Angular uncertainty estimation: (a) for 511 keV, and (b) for 1 MeV.

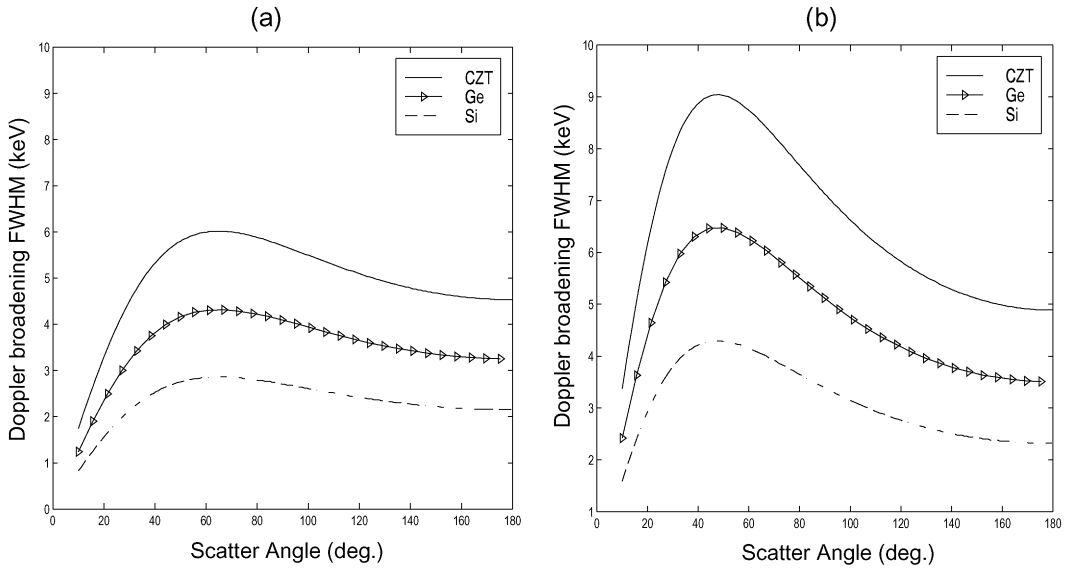

Fig. 5. Energy uncertainty due to Doppler broadening effect for: (a) 511 keV, and (b) 1 MeV.

it is obvious that the $\Delta E_{\text{Doppler}}$ increases with incident photon energy and scattering medium atomic number. For Si and Ge, the $\Delta E_{\text{Doppler}}$ is much larger than their intrinsic energy resolution, so the angular resolution due to energy uncertainty is dominated by Doppler broadening effects for incident energies above 500 keV. Thus, the excellent energy resolution of Si or HPGe detectors is not helpful for Compton imaging at middle and high γ-rays energies.

In Eq. (3), $\Delta\theta_{\text{energy}}$ is approximately proportional to $\Delta E/E_0^2$, so the energy uncertainty contribution to

angular resolution decreases with incident energy E_0. Even with the available energy resolution and large Doppler broadening for CZT, the overall angular uncertainty due to energy uncertainty at 511 keV is only around 3° for scattering angles between 20° and 80°.

3.1.3. Geometry contribution

As derived in Ref. [2], the geometry contribution to the angular uncertainty is approximately inversely proportional to the distance d between the two detectors. Since the Compton camera efficiency is inversely proportional to the square of the distance, there is a tradeoff between efficiency and angular resolution. A reasonable choice will be choosing a distance d such that $\Delta\theta^2_{\text{geometry}} \approx \Delta\theta^2_{\text{energy-resolution}} + \Delta\theta^2_{\text{Doppler}}$, so a better efficiency can be achieved while $\Delta\theta_{\text{overall}}$ is only $\sqrt{2}$ worse than that determined by the energy uncertainty components. For our CZT detectors, the lateral position resolution is around 1 mm and the depth position resolution is around 0.5 mm. As shown in Fig. 4(a) for 511 keV, when the separation distance between two voxels is 4 cm, the $\Delta\theta_{\text{geometry}}$ is comparable to $\Delta\theta_{\text{energy-resolution}}$ and $\Delta\theta_{\text{Doppler}}$. We choose the center-to-center distance between the two CZT detectors to be 5 cm so that the distance between the nearest voxels in the two detectors is 4 cm.

As shown in Fig. 4, the overall angular uncertainty $\Delta\theta_{\text{overall}}$ is 3–4° at 511 keV and reduces to 2–3° at 1 MeV for scattering angles 20–80°. So we choose the offset angle θ_c between the two detectors to be 50°. Corresponding to 20–80° scattering angles, the field of view (FOV) will be $\pm$ 30° around the axis of the first detector.

The actual angular uncertainty for the reconstructed image will be the weighted average of that shown in Fig. 4 over all acceptable scattering angles. Referring to Fig. 4, note that the $\Delta\theta_{\text{overall}}$ is a slowly varying function of scattering angle θ over the acceptable angle range 20–80°. As a result, the expected angular uncertainty for the reconstructed image will be similar to that shown in Fig. 4.

3.2. Efficiency

The intrinsic Compton scattering camera efficiency ε_{icc} is defined as the fraction of photons entering the first detector that undergo only one Compton scattering in the first detector and then undergo photoelectric absorption in the second detector. ε_{icc} for a point source can be expressed as

$$\varepsilon_{\text{icc}} = \frac{1}{\Omega_1}\int_{\text{det1}} \mathrm{d}V_1 \int_{\text{det2}} \mathrm{d}V_2\, \Delta\Omega_1 \mu_c(E_0) \mathrm{e}^{(-\mu_t(E_0)L_1)} \times \frac{\mathrm{d}\sigma}{\mathrm{d}\Omega}(\theta_{12})\Delta\Omega_2 \mathrm{e}^{(-\mu_t(E_1)L_{12})}\mu_p(E_1) \quad (6)$$

where Ω_1 is the solid angle subtended by the first detector, $\Delta\Omega_1$ is the solid angle for a differential volume element $\mathrm{d}V_1$ in the first detector, L_1 is the attenuation length in the first detector between the source and $\mathrm{d}V_1$, μ_t, μ_c, and μ_p are the total, Compton scatter, and photoelectric coefficients, respectively, L_{12} is the attenuation length between the two elements $\mathrm{d}V_1$ and $\mathrm{d}V_2$.

Analytical calculation of ε_{icc} requires numerical integration over two detector volumes and knowledge of interaction probabilities for the initial and scattered γ-rays. Instead of using an analytical approach, the Monte Carlo program EGS4 was used to calculate ε_{icc} for a point source at 10 cm from the first detector surface. We varied the incident energy from 500 keV to 3 MeV, and the results are shown in Fig. 6. For comparison, the intrinsic efficiency for a Ring Compton Camera (RCC) [6] is also shown

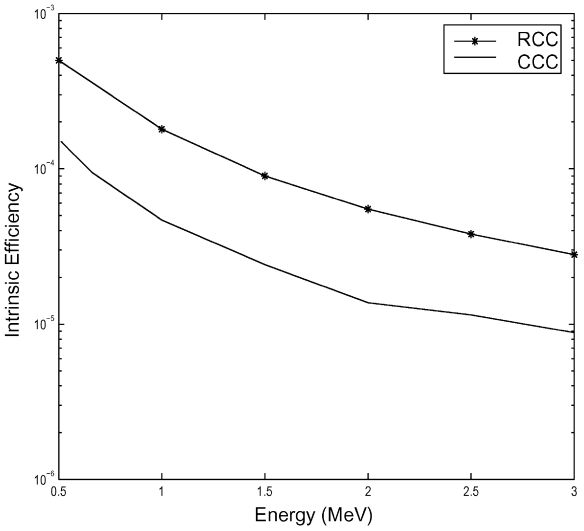

Fig. 6. Predicted CCC intrinsic efficiency.

in Fig. 6. The first detector for the RCC is a $2\times2\times0.6$ cm HPGe detector, and the second detectors consist of 16 NaI(Tl) detectors of 1.91 cm in diameter by 5.08 cm in length. The CCC has a larger atomic number, thicker first detector and reduced distance between the two detectors, but is much smaller and compact than the RCC. As a result, $\varepsilon_{\mathrm{iec}}$ is still one-fourth of that for RCC, but the angular resolution of the CCC is better than that for the RCC that varies from 5.4° at 511 keV to 4.0° at 2.75 MeV.

4. List-mode likelihood image reconstruction

Maximum-likelihood (ML) or Penalized Weighted Least-Squares (PWLS) iterative image reconstruction algorithms have been successfully used for Compton scatter imaging. In order to use the ML or PWLS algorithms, the coincident energy spectrum between two detectors must be accumulated during the data acquisition, and the system response matrix is needed for image reconstruction. For our CCC camera, there are $11\times11\times20$ voxels for each detector. Assigning just 256 channels for each detector voxel pair and only one byte for each channel, the required memory for the coincident spectra will be around 1400 MB, too large for any currently available PC. The impractical memory requirement for the system response matrix prohibits the use of any iterative reconstruction algorithm that requires a system response matrix. Therefore, list-mode data acquisition and image reconstruction are the only practical choice.

Although list mode backprojection filter (BPF) reconstruction is simple and fast, in Compton scatter imaging the intersection of the backprojected cone and the source plane is not a simple straight line as in Computerized Tomography (CT). The simple ramp filter relationship between the original image and its straight line backprojection is not accurate for Compton scatter imaging. As a result, the BPF reconstructed Compton scatter image exhibits artifacts. Another problem with BPF is that the intensity information is lost by using the ramp filter. As a result, the reconstructed image has to be renormalized by another approach to get a correct estimate of the source activities.

In the list-mode maximum likelihood reconstruction, the image reconstruction problem is treated as an estimation of a discrete source distribution $\boldsymbol{F}$ from finite measurement data sets $\{\boldsymbol{A}_j\}$. Denote the M unknown components of the discrete source distribution $\boldsymbol{F}$ as $f_1,\ldots,f_i,\ldots,f_M$, where f_i is the expected source activity in pixel i. Let the sensitivity s_i be the corresponding probability that an emitted photon from pixel i be detected as an event. The probability $P(i|\boldsymbol{F})$ for a detected event to originate from pixel i will be

$$P(i|\boldsymbol{F})=\frac{f_i s_i}{\sum_{n=1}^{M} f_n s_n}. \tag{7}$$

Represent each measurement event with attribution vector $\boldsymbol{A}$, which has seven components (interaction positions in two detectors x_1,y_1,z_1,x_2,y_2,z_2 and energy deposited in the first detector E_e). The probability density of measuring an event with attribution vector $\boldsymbol{A}$ under given source distribution $\boldsymbol{F}$ is given by

$$p(\boldsymbol{A}|\boldsymbol{F})=\sum_{i=1}^{M} p(\boldsymbol{A}|i)P(i|\boldsymbol{F}) \tag{8}$$

where $p(\boldsymbol{A}|i)$ is the probability density that a detected event generated in pixel i leads to a measurement $\boldsymbol{A}$.

Given a set of measurement $\boldsymbol{A}_1,\boldsymbol{A}_2,\ldots,\boldsymbol{A}_N$ during time T, each measurement is independent and has the identical distribution given by Eq. (8). The logarithmic likelihood of the set of measurements is

$$\begin{aligned} L(\boldsymbol{A}_1,\ldots,\boldsymbol{A}_N|\boldsymbol{F}) &= \ln p(\boldsymbol{A}_1,\ldots,\boldsymbol{A}_N|\boldsymbol{F}) \\ &= \sum_{j=1}^{N} \ln p(\boldsymbol{A}_j|\boldsymbol{F}) \\ &= \sum_{j=1}^{N} \ln\left(\sum_{i=1}^{M} P(\boldsymbol{A}_j|i)f_i s_i\right) - N\ln\left(\sum_{i=1}^{M} f_i s_i\right). \end{aligned} \tag{9}$$

The maximum likelihood estimate of the source distribution $\boldsymbol{F}$ involves finding the maximum of Eq. (9) with respect to $\boldsymbol{F}$ under the positivity constraint

$$\hat{\boldsymbol{F}}=\underset{\boldsymbol{F}\geq 0}{\operatorname{argmax}}\ L(\boldsymbol{A}_1,\ldots,\boldsymbol{A}_N|\boldsymbol{F}). \tag{10}$$

To find the ML solution, an Expectation Maximization (EM) iterative updating algorithm was

derived in Ref. [7]

$$f_l^{(t+1)} = \sum_{j=1}^{N} \frac{p(\boldsymbol{A}_j|l) f_l^{(t)}}{T \sum_{i=1}^{M} p(\boldsymbol{A}_j|i) s_i f_i^{(t)}}. \quad (11)$$

Beginning with any initial guess $\boldsymbol{F}^{(0)} \geq 0$, this algorithm converges to a global maximum of the likelihood function (9), i.e. $\boldsymbol{F}^{(\infty)} = \hat{\boldsymbol{F}}$ [7]. In any practical case, $\boldsymbol{F}^{(0)}$ can be simply set to a uniform distribution or the BPF reconstructed image. The iteration time can be controlled by a preset criteria, such as the mean square difference between two successive iterations.

By Bayes' rule, the probability density $p(\boldsymbol{A}|i)$ needed in Eq. (11) can be written as $p(\boldsymbol{A}|i) = p(\boldsymbol{A})P(i|\boldsymbol{A})/P(i)$, where $P(i) = s_i$. The conditional probability $P(i|\boldsymbol{A})$ of an event having originated from pixel i given a measured attribution vector $\boldsymbol{A}$ will be the true $P(i|\boldsymbol{A}')$ convolved with the measurement noise distribution function $p(\boldsymbol{A}'|\boldsymbol{A})$. Therefore,

$$p(\boldsymbol{A}|i)s_i = p(\boldsymbol{A}) \int P(i|\boldsymbol{A}') p(\boldsymbol{A}'|\boldsymbol{A}) \, \mathrm{d}\boldsymbol{A}' \quad (12)$$

where $\boldsymbol{A}'$ is the unknown true attribution vector for a detected event. Assuming the measurement noise distribution for each position component is an independent zero-mean Gaussian function with FWHM given by the detectors' position resolution, and the noise distribution for E_e is the convolution of a Gaussian function with known detector energy resolution with a Doppler broadened distribution, the multivariate distribution $p(\boldsymbol{A}'|\boldsymbol{A})$ is simply the product of the distributions for each component.

Given the true attribution vector $\boldsymbol{A}'$, the probability $P(i|\boldsymbol{A}')$ that the event is originated from pixel i is given by

$$P(i|\boldsymbol{A}') = \begin{cases} \dfrac{1/R_{i1}^2 \exp(-\mu_t L_{i1})}{\sum_l P(l|\boldsymbol{A}')}, & \text{when } i \text{ is on the cone defined by } \boldsymbol{A}' \\ 0, & \text{otherwise} \end{cases} \quad (13)$$

where R_{i1} is the distance between source pixel i and the interaction location in the first detector, L_{i1} is the attenuation length in first detector between them, and the μ_t is the total attenuation coefficient for incident photons.

For simplicity, the measurement noise will be neglected, i.e., $p(\boldsymbol{A}'|\boldsymbol{A}) = \delta(\boldsymbol{A}' - \boldsymbol{A})$, so Eq. (12) reduces to $p(\boldsymbol{A}|i)s_i = p(\boldsymbol{A})P(i|\boldsymbol{A}')$. The update algorithm becomes

$$f_l^{(t+1)} = \sum_{j=1}^{N} \frac{1/R_{lj1}^2 \exp(-\mu_t L_{lj1}) \delta_{lj} f_l^{(t)}/s_l}{T \sum_{i=1}^{M} 1/R_{ij1}^2 \exp(-\mu_t L_{ij1}) \delta_{ij} f_i^{(t)}} \quad (14)$$

where $\delta_{ij} = 1$ when pixel i is on the cone defined by $\boldsymbol{A}_j$, and $\delta_{ij} = 0$ otherwise.

The sensitivity s_i needed in Eq. (14) can be calculated by numerical integration or by a Monte Carlo approach before the reconstruction. In our implementation, it is approximated as

$$s_i \propto \frac{1}{R_{i1c}^2} \frac{\mathrm{d}\sigma}{\mathrm{d}\Omega}(\theta_{i12}) \mu_p, \quad (15)$$

where R_{i1c} is the distance from pixel i to the center of the first detector, θ_{i12} is the central scatter angle for pixel i, $\mathrm{d}\sigma/\mathrm{d}\Omega(\theta_{i12})$ is the corresponding Klein–Nishina Compton scattering angular cross section and μ_p is the photoelectric coefficient for the scattered photon coming from scatter angle θ_{i12}.

5. Monte Carlo simulation results

In order to verify the analytical angular resolution predictions given in Section 3.1 and test the implementation of the list-mode likelihood image reconstruction described above, the EGS4 program was used to generate simulated data for 662 keV point and spatially extended sources at a source plane 10 cm from the first detector. Gaussian noise with a corresponding FWHM for each parameter was added to the Monte Carlo generated interaction data to simulate measurement noise.

The generated data consisted of 6133 total events using 12 angular samplings covering 2π, for five point sources, located at (0,0),(0, ± 4),(± 4,0).

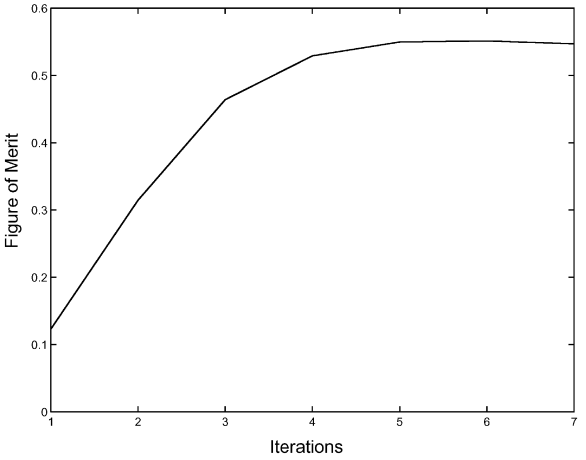

Fig. 7. Figure of merit during reconstruction iterations for the point source at the origin in Fig. 8.

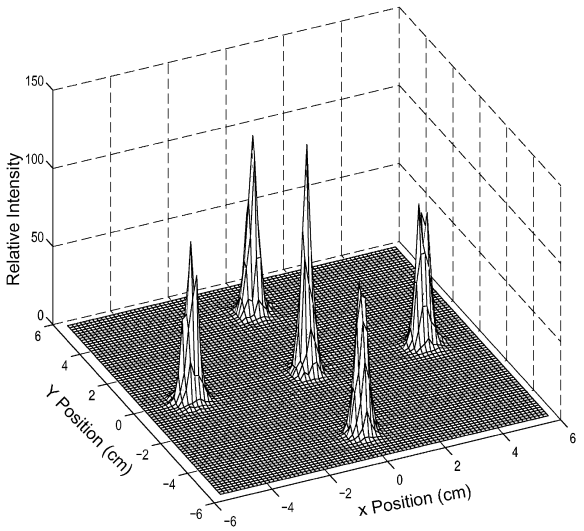

Fig. 8. Reconstructed image for 5 point sources located 10 cm from the first detector surface.

Beginning with a uniform distribution, the point spread function (PSF) figure-of-merit G^2 improves during iterations as shown in Fig. 7 for the source at the origin. The figure-of-merit improves quickly during first 3 iterations, then becomes constant after the 5th iteration. This shows the list likelihood algorithm is very efficient, requiring only 6–7 iterations for reconstruction. The reconstructed image after six iterations is shown in Fig. 8. The correct sources' location, source activities ratio and small background in the reconstructed image all indicate the reconstruction procedure is very effective. The FWHM for the on-axis source is 3.2 mm, equivalent to a 1.9° angular resolution. The average FWHM for the four off-axis sources is 4.7 mm, equivalent to 2.7°. Compared with the corresponding predicted angular resolution of 2.7° (at 50° scattering angle) and 3.2° (at 70° scattering angle) for 662 keV, the simulation results are slightly better than the predictions. Considering that the simulation does not include the Doppler broadening

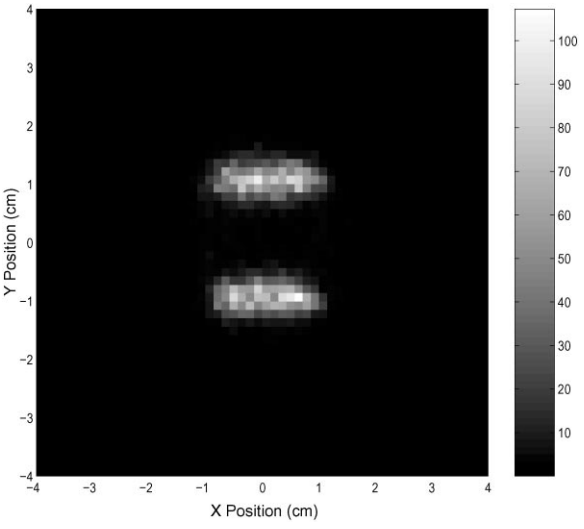

Fig. 9. Reconstructed image for two 1 cm long line sources.

effects, and using a 5 cm separation between the two detectors centers implies that the interaction locations for most events will be larger than 4 cm, the simulation and analytical predictions agree well.

Fig. 9 is the reconstructed image for two 1 cm line sources using 7121 simulated events. The average FWHM for the two lines along the y direction is 4.4 mm ($\approx 2.5°$), which is similar to FWHM for

[2] PSF figure-of-merit G is defined as [8]

$$G = \frac{\max[f(n_1, n_2)]}{[\sum_{n1}\sum_{n2}|f(n_1, n_2)|^2]^{(1/2)}}$$

where n_1, n_2 are 2-D pixel indexes within the PSF. The G incorporates the entire PSF in the resolution measure, unlike FWHM which only gives the resolution along a line. For an ideal delta function PSF, $G = 1$.

the point sources in Fig. 8. The signal-to-noise ratio in the reconstructed image (SNR_{ccc}) on the two lines is 3.37. Since the interaction data is simulated by a Monte Carlo program, the source location for each simulated event is known and the true signal to noise ratio (SNR_{true}) is 15.28 for the corresponding data set. The encoding penalty is equal to the ratio $SNR_{true}/SNR_{ccc} = 4.5$. Thus, in order to have same signal-to-noise ratio as a perfect mechanically collimated camera, the efficiency of the CCC must be 20 times higher.

6. Summary

Based on our measured detector energy and position resolutions, the performance of a Compton scattering camera using two 3-D position sensitive 1 cm^3 cubic CZT detectors is evaluated. Using currently available detector energy resolutions, the CZT detector should not be used as the first detector for Compton scatter imaging at low energy. Comparing angular resolution and efficiency, CZT detectors with 3-D position sensitivity are superior to silicon and HPGe for several hundred keV to a few MeV for Compton imaging. They are also advantageous as portable devices. For a central scatter angle of 50° and a 5 cm separation between the two detectors, the angular resolution is predicted to be 3–4° for 511 keV γ-rays within a $\pm 30°$ FOV, and improves to $\sim 2°$ at 1 MeV. The intrinsic efficiency of the camera ranges between 1.5×10^{-4} and 8.8×10^{-6} for 511 keV–3 MeV.

The reconstructed images using the list likelihood iteration algorithm and Monte Carlo simulated data yielded similar angular resolutions for point distributed sources and spatially extended line sources. The results agree well with the analytical predictions. The signal-to-noise ratio for the reconstructed image of two lines is 4.5 times worse than the source SNR at 662 keV. This implies the CCC camera must be 20 times more efficient than a perfect mechanically collimated camera to achieve the same SNR at this energy.

Acknowledgements

This work was supported under US Department of Energy, Grant No. DE-FG07-98ID13645.

References

[1] Z. He, W. Li, G.F. Knoll, D.K. Wehe, J. Berry, C.M. Stahle, Nucl. Instr. and Meth. A 422 (1999) 173.
[2] M. Singh, Med. Phys. 10 (4) (1983) 421.
[3] M.J. Copper, Contemp. Phys. 18 (5) (1977) 489.
[4] R. Cesareo et al., Phys. Rep. 213 (3) (1992) 117.
[5] F. Biggs, L.B. Mendelsohn, J.B. Mann, Atom. Data Nucl. Data Tables 16 (1975) 201.
[6] J.B. Martin, N. Dogan, J.E. Gormley, G.F. Knoll, M. O'Donell, D.K. Wehe, IEEE Trans. Nucl. Sci. 41 (4) (1994) 1019.
[7] L. Parra, H.H. Barrett, IEEE Trans. Med. Imaging 17 (2) (1998) 228.
[8] S.J. Norton, M. Lionzer, Ultrason. Imaging 1 (1979) 154.